



Deconvolving distribution of relaxation times, resistances and inductance from electrochemical impedance spectroscopy via statistical model selection: Exploiting structural-sparsity regularization and data-driven parameter tuning



Xin Li ^{a, b, *}, Mahshid Ahmadi ^c, Liam Collins ^{a, b}, Sergei V. Kalinin ^{a, b, **}

^a Center for Nanophase Material Sciences, Oak Ridge National Laboratory, USA

^b Institute for Functional Imaging of Materials, Oak Ridge National Laboratory, USA

^c Joint Institute for Advanced Materials, Material Science and Engineering Department, University of Tennessee, USA

ARTICLE INFO

Article history:

Received 1 March 2019

Received in revised form

30 April 2019

Accepted 3 May 2019

Available online 10 May 2019

ABSTRACT

The distribution of relaxation times (DRT) has drawn increasing attention for interpreting electrochemical impedance spectroscopy (EIS). Deconvolution of DRT from EIS is a challenging ill-posed problem that requires regularization methods. In this work, we formulate DRT reconstruction task as a statistical model selection problem with structural-sparsity penalties. We utilize the Elastic net regularization that simultaneously benefits from Ridge and Lasso regularizations with optimal tuning parameter automatically determined by the information criteria. We benchmark our approach on four synthetic experiments (a ZARC element, ZARC mixtures, a RC circuit and a Fractal element) and two real EIS datasets of a Lithium ion battery and an organic-inorganic halide class of perovskites in oxygen environment at different gas pressures. We demonstrate the superiority of proposed model selection procedure, that is capable of eliminating pseudo peaks and representing asymmetries in DRT as well as precisely estimating resistances. We highlight our approach is robust to reducing and subsampling EIS frequency range, making it a promising tool for timing-resolved, localized and large scale EIS data analysis. For the Lithium ion battery data analysis, we extend the classical DRT model to incorporate the inductive effect and illustrate DRT as a guidance for equivalent circuit modeling to refine impedance reconstruction at low risks of overfitting. Furthermore, the structural-sparsity regularization could be extended for multidimensional and Bayesian EIS data analysis.

© 2019 Elsevier Ltd. All rights reserved.

1. Introduction

Electrochemical impedance spectroscopy (EIS) [1,2] has become the main stay for multiple timescales characterization on many electrochemical systems such as fuel cells [3,4], lithium-ion batteries [5,6], solar cells [7,8] and bioanalytical applications [9]. Nonetheless, interpreting physically relevant phenomena from EIS is challenging. A typical approach of analyzing EIS spectral is fitting the impedance data against equivalent circuits models (ECM) via

the nonlinear least squares (CNLS) procedure [10–14]. Several groups have made significant contributions towards mapping EIS spectrum to transport phenomena and reaction kinetics [15–23].

As an alternative for analyzing EIS data, distribution of relaxation times (DRT) has recently draw much attention [24,25]. DRT is a model independent approach that emphasizes the distribution of EIS timescales, consisting of peaks with different widths whose locations define the major time constants of the system under study. Mathematically, DRT is connected to the EIS via the following convolution equation [26–29]:

$$Z(f) = R_\infty + R_p \int_0^\infty \frac{g(\tau)}{1 + i2\pi f\tau} d\tau \quad (1)$$

where $Z(f)$ is the measured impedance data at given frequencies f ,

* Corresponding author. Center for Nanophase Material Sciences, Oak Ridge National Laboratory, USA.

** Corresponding author. Center for Nanophase Material Sciences, Oak Ridge National Laboratory, USA.

E-mail addresses: lix3@ornl.gov (X. Li), sergei2@ornl.gov (S.V. Kalinin).

Symbols	
R_∞	High frequency cut-off resistance
L_0	Inductance element
R_p	Polarization resistance
f	EIS sampling frequency
τ	Relaxation time
$g(\tau)$	Distribution function of relaxation times
ψ_m	Kernel function
β_m	Kernel weight
Z'	Real impedance vector
Z''	Imaginary impedance vector
A'	Kernel basis matrix of DRT for the real impedance vector
A''	Kernel basis matrix of DRT for the imaginary impedance vector
β	Kernel weights vector
$\tilde{\beta}$	Relaxed kernel weights vector
$\hat{\beta}^*$	Augmented kernel weights vector
Z^*	Augmented imaginary impedance vector
A^*	Augmented kernel basis matrix for imaginary EIS data
A^+	Moore–Penrose inverse of A^*
λ_1	Selection tuning parameter in elastic net regularization
λ_2	Shrinkage tuning parameter in elastic net regularization
C_p	Mallow's Cp criterion

R_∞ is the high frequency cut-off resistance, R_p is the polarization resistance and $g(\tau)$ is the possibility density function of time relaxation characteristics that subjects to $\int_0^\infty g(\tau) = 1$. Since EIS frequency are usually sampled logarithmically, equation (1) is often rewritten in terms of possibility density function of $\ln \tau$, denoted as $G(\tau)$. Via the change of variable trick:

$$\tau = f(\ln \tau) = e^{\ln \tau}, \quad d\tau = f'(\ln \tau) d\ln \tau = e^{\ln \tau} d\ln \tau = \tau d\ln \tau \quad (2)$$

we can see $G(\tau) = \tau g(\tau)$,

$$G(\tau) = f'(\ln \tau) g(f(\ln \tau)) = e^{\ln \tau} g(e^{\ln \tau}) = \tau g(\tau) \quad (3)$$

substituting equations (2) and (3) into equation (1), we have:

$$\begin{aligned} Z(f) &= R_\infty + R_p \int_0^\infty \frac{g(\tau)}{1 + i2\pi f \tau} d\tau \\ &= R_\infty + R_p \int_{-\infty}^\infty \frac{G(\tau)}{\tau} \frac{1}{1 + i2\pi f \tau} \tau d\ln \tau \\ &= R_\infty + R_p \int_{-\infty}^\infty \frac{G(\tau)}{1 + i2\pi f \tau} d\ln \tau \end{aligned} \quad (4)$$

Various methods for deconvoluting $G(\tau)$ from EIS spectra have been proposed, including Fourier transform (FT) [28,30], maxim entropy [31], Monte Carlo methods [32,33], genetic programming [34,35] and Ridge regression (also known as Tikhonov Regularization) [36–40].

Unfortunately, deconvolution of $G(\tau)$ from $Z(f)$ is notoriously known as an ill-posed inverse problem meaning there are many possible solutions for $G(\tau)$. For example, pseudo peaks sometimes appear in estimated DRT (In terms of ECM analysis, multiple models may yield almost identical EIS responses [2,41]). It requires much effort to adjust tuning parameters in these methods to get an agreeable DRT reconstruction. Pioneering work of Ciucci group [37] proposed real and imaginary cross-validation test functions to address the issue of selecting the regularization parameter, compared the effects of Ridge regularization (favoring smoothness in DRT) and Lasso regularization (favoring sparsity in DRT) and concluded that Lasso should be used in conjunction with Ridge regression. As pointed out in a recent review [42], statistical analysis could become a powerful tool for justifying the quality of evaluating DRT.

In this work, we propose a solving procedure for both DRT $G(\tau)$ and resistances R_∞, R_p and possible inductance effects, based on the Elastic Net regularization that simultaneously utilizes Ridge and

Lasso Regression, with optimal tuning parameter selected automatically based on information criteria. In addition, non-negativity of DRT is guaranteed during computation, since naive implementation of Ridge and Lasso regularization may yield negative $G(\tau)$ values. Our approach is capable of excluding pseudo peaks and representing asymmetry in $G(\tau)$ as well as accurately estimating R_∞ and R_p . We demonstrate that estimation accuracy is robust to the reduction of EIS frequency sampling density and range, making it promising for advanced EIS techniques, such as timing-resolved [43–45], localized [46–48] and the atomic force microscopy based impedance spectroscopy [49–51], where EIS frequency sampling range and density may be compromised by the spatial-temporal resolution and probe size. The benefits of structural-sparsity (Elastic net regularization) could also be extended for multidimensional EIS data analysis [52] and be explored under Bayesian analysis of EIS data [53,54] via the spike and slab priors [55].

2. Theory

We approximate probability density $G(\tau)$ in the following form of a kernel density estimation,

$$G(\tau) = \sum_{m=1}^M \beta_m \psi_m(\tau) \quad (5)$$

where ψ_m is the m th kernel function that satisfies $\int \psi_m(\tau) d\tau = 1$, and β_m is the corresponding kernel weight. The unknown coefficient $\beta_m \geq 0$ determines the weight of m th kernel and subjects to $\sum_m \beta_m = 1$ for $G(\tau)$ being a probability density function. Here we consider a popular choice of the kernel function ψ_m , a step function (additional investigation on choices of kernel functions for deconvoluting density function can be found in [38,56]).

$$\psi_m(\tau) = \frac{1}{\tau_{m+1} - \tau_m} \mathcal{I}_{[\tau_m, \tau_{m+1}]}(\tau) \quad (6)$$

where $\mathcal{I}_{[\tau_m, \tau_{m+1}]}$ is an indicator function defined at range $[\tau_m, \tau_{m+1}]$. To reduce the risk of missing potential peaks in $G(\tau)$, we consider a large range of τ . The values of τ range from microsecond (10^{-6}) to megasecond (10^6) logarithmically. Substituting equation (5) into equation (4), we then have equation (4) into a mixture form. In addition, we consider the experimental EIS spectrum is a noisy version of theoretical data:

$$\begin{aligned} Z(f) = & R_\infty + R_p \sum_{m=1}^M \beta_m \int_{-\infty}^{\infty} \frac{\psi_m(\tau)}{1 + (2\pi f \tau)^2} d \ln \tau + \\ & -i R_p \sum_{m=1}^M \beta_m \int_{-\infty}^{\infty} 2\pi f \tau \frac{\psi_m(\tau)}{1 + (2\pi f \tau)^2} d \ln \tau + \varepsilon \end{aligned} \quad (7)$$

where ε is the experiment and discretization noise. Estimation of $G(\tau)$, R_p , R_∞ can be pursued by maximizing the likelihood of above function, which is equivalent to minimize following sum of squares:

$$\text{Minimize } \|Z' - \mathbf{1}R_\infty - R_p \mathbf{A}' \beta\|_2^2 + \|Z'' - R_p \mathbf{A}'' \beta\|_2^2 \quad (8)$$

where $\mathbf{A}', \mathbf{A}''$ are the real- and imaginary-part of the covariate matrix \mathbf{A} of size $N \times M$, whose element $\mathbf{A}_{nm} = \int \frac{\psi_n(\tau)}{1 + i2\pi f_n \tau} d \ln \tau$; the integration can be calculated using the Monte Carlo approximation with sample size K ,

$$\int \frac{\psi_m(\tau)}{1 + i2\pi f_n \tau} d \ln \tau \approx \frac{1}{K} \sum_{k=1}^K \frac{1}{1 + i2\pi f_n \tau^{(k)}} \quad (9)$$

where $\tau^{(k)}$ is a random sample from the density kernel $\psi_m(\tau)$. We set a sufficiently large sample size for numerical convergence.

Note that the imaginary-part data fidelity term $\|Z'' - R_p \mathbf{A}'' \beta\|_2^2$ in equation (8) are only involved with R_p and β , we first utilize imaginary part of EIS spectrum to estimate R_p and β . Columns of the covariate matrix \mathbf{A}'' suffers from high degree of collinearity. For example, Fig. 1 shows the correlations (absolute value) among columns of \mathbf{A}'' . The high correlations imply that multiple regression coefficients in β have almost indistinguishable effects, yielding non-unique solutions to equation (8). To address the collinearity issue, we propose to use the Elastic Net [57] consisting of double penalizations with L_1 norm and L_2 norm,

$$\text{Minimize } \|Z'' - \mathbf{A}'' \tilde{\beta}\|_2^2 + \lambda_1 \|\tilde{\beta}\|_1 + \lambda_2 \|\tilde{\beta}\|_2^2 \quad (10)$$

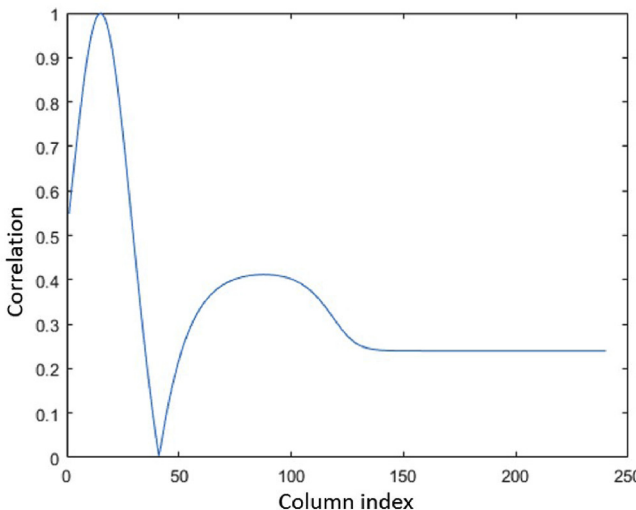


Fig. 1. Correlations between 15th column of \mathbf{A}'' and all columns of \mathbf{A}'' .

where we introduce the relaxed variable,

$$\tilde{\beta} = R_p \beta, \quad R_p = 1^T \tilde{\beta} \quad (11)$$

λ_1 and λ_2 in equation (10) are selection and shrinkage tuning parameters. Traditional cross-validation on the two dimensional grid of (λ_1, λ_2) is computationally heavy and may present some challenges in EIS context because of the small data set's size [37]. Instead, we first use the non-negative least angle regression algorithm (LARS) [58,59] that implicitly select optimal λ_1 based on information criteria, given a fixed λ_2 . Specifically, LARS solves equation (10) in the data augmentation form [57],

$$\text{Minimize } \left\| \mathbf{Z}^* - \mathbf{A}^* \tilde{\beta}^* \right\|_2^2 + \frac{\lambda_1}{\sqrt{1 + \lambda_2}} \left\| \tilde{\beta}^* \right\|_1 \quad (12)$$

where

$$\mathbf{A}^* = (1 + \lambda_2)^{-1/2} \left(\frac{\mathbf{A}''}{\sqrt{\lambda_2} \mathbf{I}} \right), \quad \mathbf{Z}^* = \begin{pmatrix} \mathbf{Z}'' \\ 0 \end{pmatrix} \quad (13)$$

and

$$\tilde{\beta} = \sqrt{1 + \lambda_2} \beta^* \quad (14)$$

The LARS algorithm is an iterative solver that sequentially generates $\tilde{\beta}^*$ solution path for implicit λ_1 values in a decreasing sequence ($\infty \rightarrow 0$). The optimal $\tilde{\beta}^*$ in the LARS solution path corresponds to the iteration that has the minimal value of Mallows's C_p criterion [60].

$$C_p = \frac{(\mathbf{Z}^* - \mathbf{A}^* \tilde{\beta}^*)^T (\mathbf{Z}^* - \mathbf{A}^* \tilde{\beta}^*)}{\sigma^2} - N + 2 \left\| \tilde{\beta}^* \right\|_0 \quad (15)$$

where σ^2 is the mean square error of low-bias model,

$$\sigma^2 = \frac{(\mathbf{Z}^* - \mathbf{A}^* \mathbf{b})^T (\mathbf{Z}^* - \mathbf{A}^* \mathbf{b})}{N} \quad (16)$$

with $\mathbf{b} = \mathbf{A}^+ \mathbf{Z}^*$ where \mathbf{A}^+ is the Moore–Penrose inverse of \mathbf{A}^* . During the iterations of LARS algorithm, C_p value should decrease at first, as the mean square error term generally decreases, then C_p value would rebound later due to the increasing degrees of freedom. Fig. 2 is an example of the trend of C_p from the Lithium-ion battery EIS data analysis in later sections.

With optimal $\tilde{\beta}^*$ obtained at the LARS iteration with minimal C_p value, we immediately get the estimates of β , R_p via equations (14) and (11). Then optimal R_∞ can be solved via the first-order necessary condition of real-part data fidelity term $\|Z' - \mathbf{1}R_\infty - R_p \mathbf{A}' \beta\|_2^2$ in equation (8),

$$R_\infty = \frac{\sum_{n=1}^N (Z')_n - \sum_{n=1}^N (R_p \mathbf{A}' \beta)_n}{N} \quad (17)$$

For a fixed λ_2 value, we follow above procedure to get estimates of β , R_p , and R_∞ . We perform a grid search of λ_2 to choose the one that gives the minimum sum of squares in equation (8).

3. Results

We tested our approach for four synthetic experiments (a ZARC

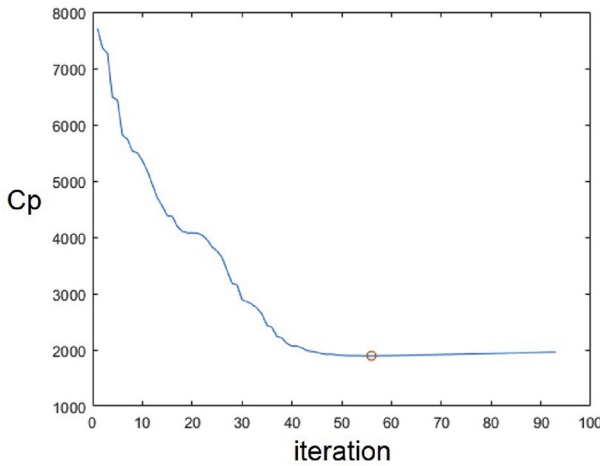


Fig. 2. An example of C_p estimates during LARS algorithm iterations for the Lithium-ion battery EIS data analysis in later sections. Red circle indicates the minimal. (For interpretation of the references to colour in this figure legend, the reader is referred to the Web version of this article.)

element, ZARC mixtures, a RC circuit and a Fractal element) and two real EIS datasets of (a) Lithium ion battery and (b) organic-inorganic halide class of perovskites in oxygen environment at different gas pressures. We emphasize that all the following reconstructions are automatically determined by the statistical model selection procedure without manual efforts of tuning parameters.

3.1. Synthetic experiments

For each synthetic model, we analyzed three data sampling strategies: (1) a normal range of EIS spectrum, $10^{-1}\text{Hz} < f_n < 10^6\text{Hz}$, with 10 points per decade (ppd); (2) normal range, but with only 5 ppd; (3) half frequency range, $10^0\text{Hz} < f_n < 10^{3.5}\text{Hz}$, with 10 ppd.

3.1.1. ZARC element

The ZARC circuit serially consists of a resistance (R_∞) and a parallel connection of a constant phase element and a resistor (R_p). The impedance of a single ZARC element is given by:

$$Z(f) = R_\infty + \frac{R_p}{1 + (i2\pi f\tau_0)^\phi} \quad (18)$$

where we set $R_\infty = 5\Omega$, $R_p = 40\Omega$, $\tau_0 = 0.01\text{s}$ and $\phi = 0.55$. The analytical DRT for a ZARC element is a log-normal distribution [36,61]:

$$G(\tau) = \tau g(\tau) = \frac{1}{C} \frac{R_p}{2\pi} \frac{\sin((1-\phi)\pi)}{\cosh(\phi \ln(\tau/\tau_0)) - \cos((1-\phi)\pi)} \quad (19)$$

where C is the normalization constant to make $G(\tau)$ a probability density function. Fig. 3 displays analytical EIS and DRT, together with the fitted EIS and estimated $G(\tau)$, R_p , R_∞ . For all three data collection strategies, the fitted EIS and DRT matches well to the analytical ones; there is no pseudo peak in the estimated DRTs; both resistances values can be accurately estimated. The reconstruction performances are robust to reducing and subsampling EIS frequency range.

3.1.2. ZARC mixtures

The analytical impedance from the ZARC mixtures model is given by:

$$Z(f) = R_\infty + \sum_{m=1}^M \frac{R_m}{1 + (i2\pi f\tau_m)^{\phi_m}} \quad (20)$$

where R_m , τ_m and ϕ_m characterize m th ZARC element. There is a discrepancy between equation (20) and the DRT convolution model in equation (1) where individual R_m is implicitly contained in $G(\tau)$. To estimate R_m , we rewrite equation (20) in a consistent form with convolution model in equation (1),

$$Z(f) = R_\infty + R_p \sum_{m=1}^M \frac{w_m}{1 + (i2\pi f\tau_m)^{\phi_m}} \quad (21)$$

where $R_p = \sum_{m=1}^M R_m$ and $w_m = \frac{R_m}{R_p}$ is the weight for each ZARC element. Via equation (21), estimated R_p should reflect the total polarization resistance of ZARC mixtures model meanwhile individual R_m can be estimated by the heights of the peaks (p_1, p_2, \dots, p_m) in reconstructed DRT via $R_m = R_p \frac{p_m}{\sum_{m=1}^M p_m}$.

We consider mixture models consisting of two ZARC elements with equal and non-equal weights respectively. For both models, we set $R_\infty = 10\Omega$, $\phi_1 = \phi_2 = 0.7$ and $\tau_1 = 0.001\text{s}$, $\tau_2 = 0.1\text{s}$. For equal weights, we set $R_1 = R_2 = 50\Omega$. For non-equal weights, we set $R_1 = 50\Omega$, $R_2 = 30\Omega$. Figs. 4 and 5 show the reconstruction performances for above cases where all variables R_∞, R_1, R_2 and $G(\tau)$ can be accurately estimated. Estimation accuracy of R_1, R_2 slightly decreases (Figs. 4f and 5f) under the very limited data sampling of half frequency range with 10 ppd.

3.1.3. RC circuit

The EIS spectra from a single RC circuit is derived as

$$Z(f) = R_\infty + \frac{R_p}{1 + i2\pi fR_pC} \quad (22)$$

where we set $R_\infty = 1\Omega$, $R_p = 1\Omega$ and $C = 1\text{F}$. The analytical DRT for a RC circuit is a Dirac distribution centered at $\tau = R_pC = 1\text{s}$.

Fig. 6 shows the reconstruction performances for the RC circuit model. For EIS spectra with normal range (10 ppd and 5 ppd), the estimated DRT consists of a single sharp peak centered at 1s. For EIS of half range with 10 ppd, the estimated DRT has a single sharp peak at 0.223s. R_∞ and R_p were also accurately estimated, except for EIS spectral of half frequencies with 10 ppd where estimations of EIS spectra and R_p have relatively larger errors compared to other two data collection cases. Also we note that slight asymmetries exist in the estimated DRTs. One possible reason is that analytical form of EIS spectrum for a RC circuit can be numerically treated as a special case of the Fractal element discussed next.

3.1.4. Fractal element

The EIS response for a Fractal element [36,62] is given by,

$$Z(f) = R_\infty + \frac{R_p}{(1 + i2\pi f\tau_0)^\phi} \quad (23)$$

where we set $R_\infty = 10\Omega$, $R_p = 10\Omega$, $\phi = 0.6$ and $\tau_0 = 0.1\text{s}$. Note that, when $\phi = 1$, the Fractal element reduces to the RC circuit. The analytical DRT for a Fractal element has a singularity point at τ_0 where asymmetry and discontinuity occur. The analytical DRT of a

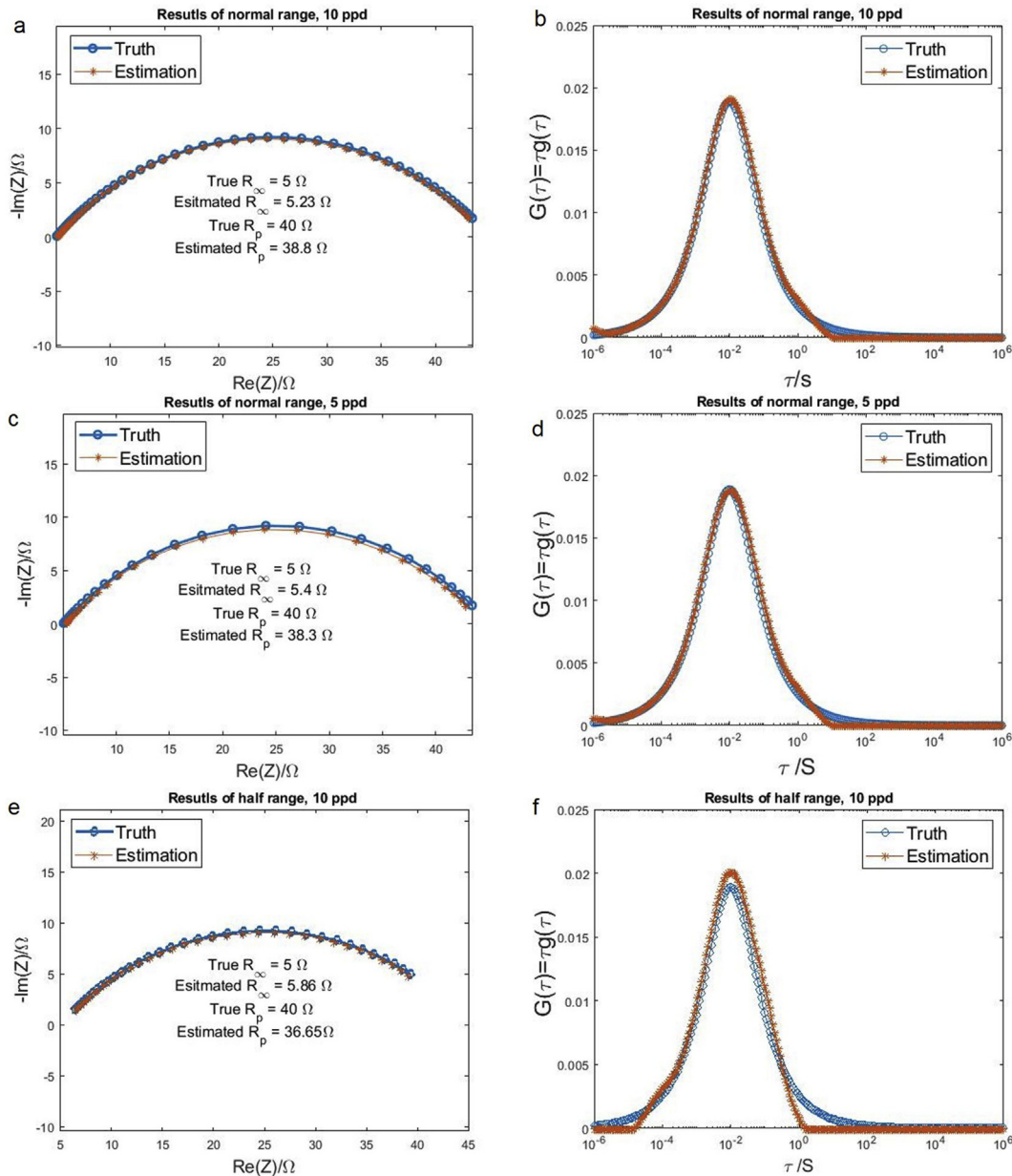


Fig. 3. Reconstructions of a ZARC element. (a,c,e) Analytical and estimated EIS spectra and resistances for the three data collection strategies: normal range with 10 ppd, normal range with 5 ppd, half range with 10 ppd. (b,d,f) Analytical and estimated DRTs, corresponding to the three data collection strategies.

Fractal element is given by,

$$G(\tau) = \tau g(\tau) = \begin{cases} R_p \frac{\sin(\phi\pi)}{\pi} \left(\frac{\tau}{\tau_0 - \tau} \right)^{\phi}, & \text{if } \tau \leq \tau_0 \\ 0, & \text{if } \tau > \tau_0 \end{cases} \quad (24)$$

Fig. 7 shows the reconstruction results for the Fractal element under the three data collection strategies. Since the analytical $G(\tau) \rightarrow \infty$ as $\tau \rightarrow \tau_0$, for visualization purposes, we normalized analytical $G(\tau)$ in Fig. 7. For all three sampling strategies, both R_∞ and R_p were accurately estimated. All three reconstructed DRTs display a single asymmetric peak at singularity point $\tau = 0.07$, although the asymmetry is weakened under half frequency range with 10 ppd case.

3.2. Experimental lithium ion battery EIS data analysis

In this section we tested the model selection approach on a real EIS response of a commercial lithium ion battery (LiCoO₂ Ansmann 18650) at the states of charge 25%, collected at room temperature. The DRT analysis of this EIS data has been conducted via frequentist (Ridge and Lasso regression) [37,38] and Bayesian settings [53,54]. Specifically, the original Lithium ion battery EIS data comes from the opensource software introduced in [38].

The sampling frequency f for original EIS data ranges from 999 Hz to 5 mHz with 107 sampling points in total. For the real EIS data case, we considered four data collection strategies: (1) the original EIS data; (2) full frequency range with half sampling density, yielding 54 sampling points; (3) truncated frequency range from 316 Hz to 16 mHz with 87 sampling points and (4) truncated frequency range (316 Hz–16 mHz) with half sampling density,

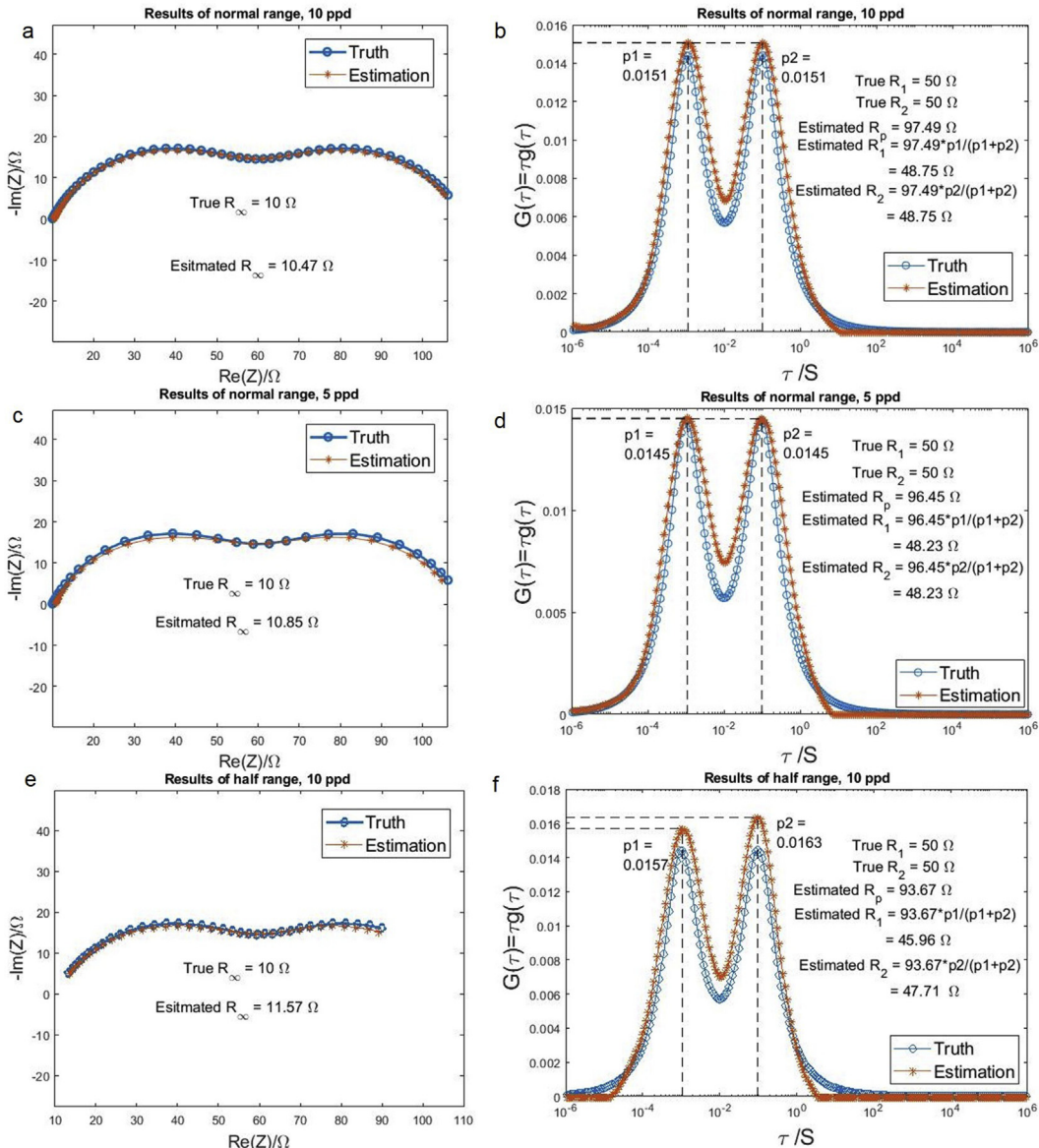


Fig. 4. Reconstructions of ZARC mixtures with equal weights. (a,c,e). Analytical and estimated EIS spectra and resistances for the three data collection strategies: normal range with 10 ppd, normal range with 5 ppd, half range with 10 ppd. (b,d,f) Analytical and estimated DRTs and resistances, corresponding to the three data collection strategies.

yielding 44 sampling points.

In Fig. 8, the reconstruction results are presented for the four data collection scenarios. Reducing the number of points per decade has minor influence on the reconstruction. Estimation values of resistances are stable under four data sampling strategies. For full frequency range (10 ppd and 5 ppd), the estimated DRTs consist of three peaks at $\tau = 0.003\text{s}, 0.157\text{s}, 32.77\text{s}$ with highest peak located at rightmost. For reduced range (10 ppd and 5 ppd), the estimated DRTs consist of three peaks at $\tau = 0.003\text{s}, 0.157\text{s}, 12.95\text{s}$ with highest peak in the middle.

Estimated DRTs here for the Lithium ion battery are consistent with the optimal DRT representation reported earlier by external manual validations. In [37], Re-Im cross-validation criterion and Lasso yielded pseudo peaks and Re-Im discrepancy provided a suitable DRT on truncated τ domain (10^{-3}s to 10^3s) that is similar to Fig. 8b,d. Similar results can be found by the radial basis function (RBF) method [38] with manual tuning of the Ridge shrinkage parameter. Also, estimated DRT in Fig. 8b,d are consistent with the

posterior distributions reported by the Bayesian analysis framework [53,54]. In addition, the estimated DRT under reduced frequency range (Fig. 8f,h) match well with the analytical DRT (with highest peak in the middle) via a 3-ZARC ECM fit of the EIS data, that was treated as a reference in [54]. The discrepancy in $G(\tau)$ may be connected to the degree of fitness of the EIS data: for full range cases (Fig. 8a,c), there is a larger fitting error in the high frequency domain, compared to the reduced range cases (Fig. 8e,g), which may be caused by the larger system error introduced by instrumentation at high frequencies. Combining analysis here with earlier work [37,38,53,54], the EIS practitioner may conjecture that the EIS data has inherent noise, especially in the high frequency domain.

3.2.1. Estimating inductance effect

The positive imaginary values at high frequency range of EIS spectrum in Fig. 8a could be possibly due to the inductance effect. The classical formalism linking EIS spectrum and DRT by equation

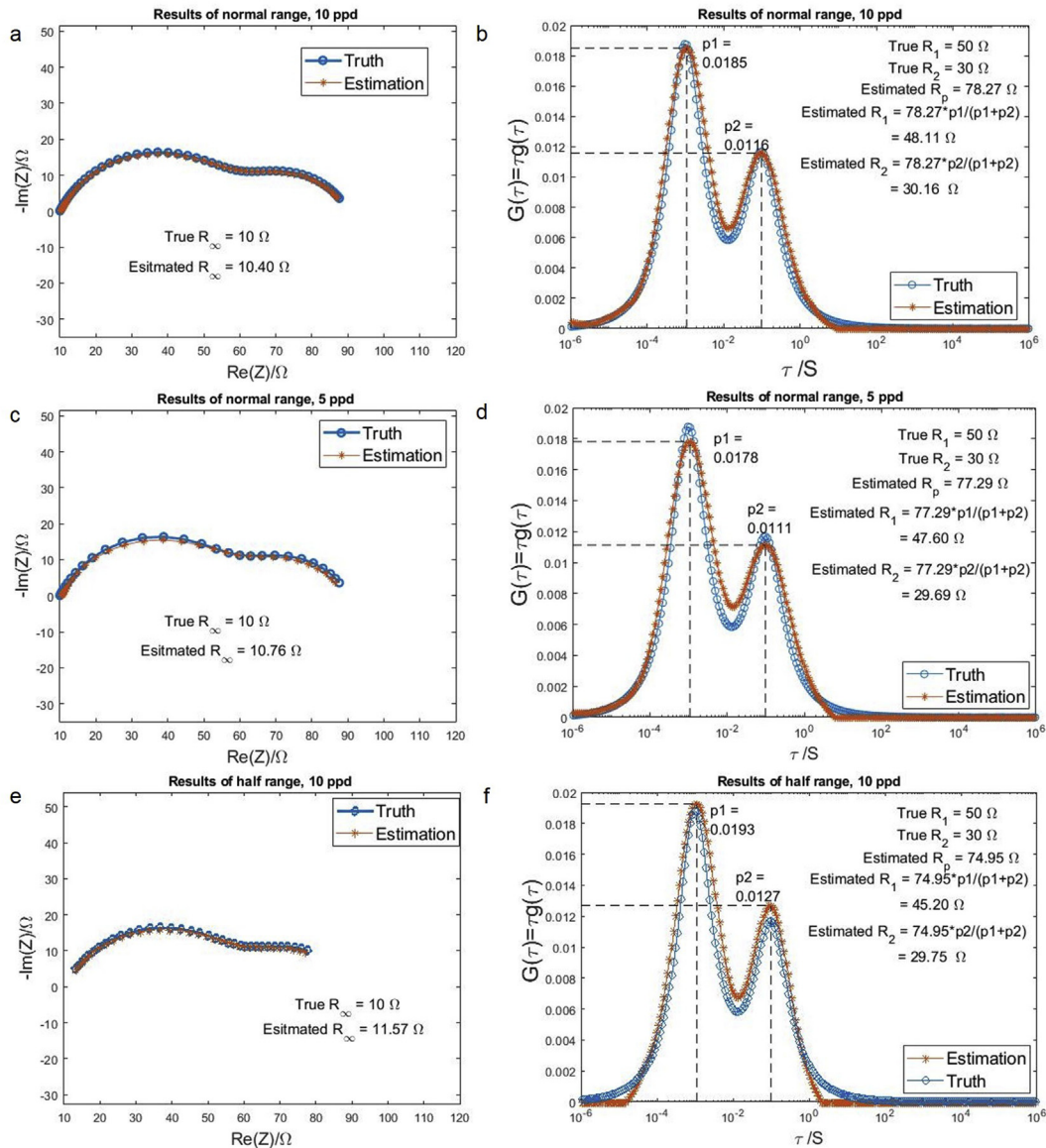


Fig. 5. Reconstructions of ZARC mixtures with non-equal weights. (a,c,e) Analytical and estimated EIS spectra and resistances for the three data collection strategies: normal range with 10 pfd, normal range with 5 pfd, half range with 10 pfd. (b,d,f) Analytical and estimated DRTs and resistances, corresponding to the three data collection strategies.

(1) only consists of resistance and capacitance elements, and is unsuitable for impedance containing inductive component at high frequencies [24]. Trying to overcome this limitation, we expand the classical formalism by adding an inductive element, which is also adopted in the recent review [42]:

$$Z(f) = R_\infty + i2\pi f L_0 + R_p \int_{-\infty}^{\infty} \frac{G(\tau)}{1 + i2\pi f \tau} d \ln \tau \quad (25)$$

where L_0 is an inductance. Correspondingly, the model estimator for the imaginary-part of EIS spectrum in equation (10) is extended to,

$$\text{Minimize } \left\| \mathbf{Z}'' - 2\pi \mathbf{f} L_0 - \mathbf{A}'' \tilde{\beta} \right\|_2^2 + \lambda_1 \left\| \tilde{\beta} \right\|_1 + \lambda_2 \left\| \tilde{\beta} \right\|_2^2 \quad (26)$$

$[L_0, \tilde{\beta}]$ can be estimated via block-wise coordinate descent: starting with initial guess of $L_0^{(0)} = 0$, at each iteration i , we update $\tilde{\beta}^{(i)}$ and

$L_0^{(i)}$ sequentially:

$$\tilde{\beta}^{(i)} = \underset{\tilde{\beta}}{\operatorname{argmin}} \left\| \mathbf{Z}'' - 2\pi \mathbf{f} L_0^{(i-1)} - \mathbf{A}'' \tilde{\beta} \right\|_2^2 + \lambda_1 \left\| \tilde{\beta} \right\|_1 + \lambda_2 \left\| \tilde{\beta} \right\|_2^2 \quad (27)$$

$$L_0^{(i)} = \underset{L_0}{\operatorname{argmin}} \left\| \mathbf{Z}'' - \mathbf{A}'' \tilde{\beta}^{(i)} - 2\pi \mathbf{f} L_0 \right\|_2^2 \quad (28)$$

equation (27) is solved by the same non-negative LARS procedure as described in section 2 and equation (28) is solved by non-negative least square [63]. Estimates of L_0 converge after several iterations, see Fig. 9 for an example.

Fig. 10 shows the fitting results of the full Lithium ion battery EIS spectrum, by the extended model. The goodness of fit was much improved especially for the high-frequency range of EIS spectrum, with estimated $L_0 = 0.62 \mu H$. We also tested extended formalism with non-inductive EIS datasets. Reconstructions of EIS spectrum

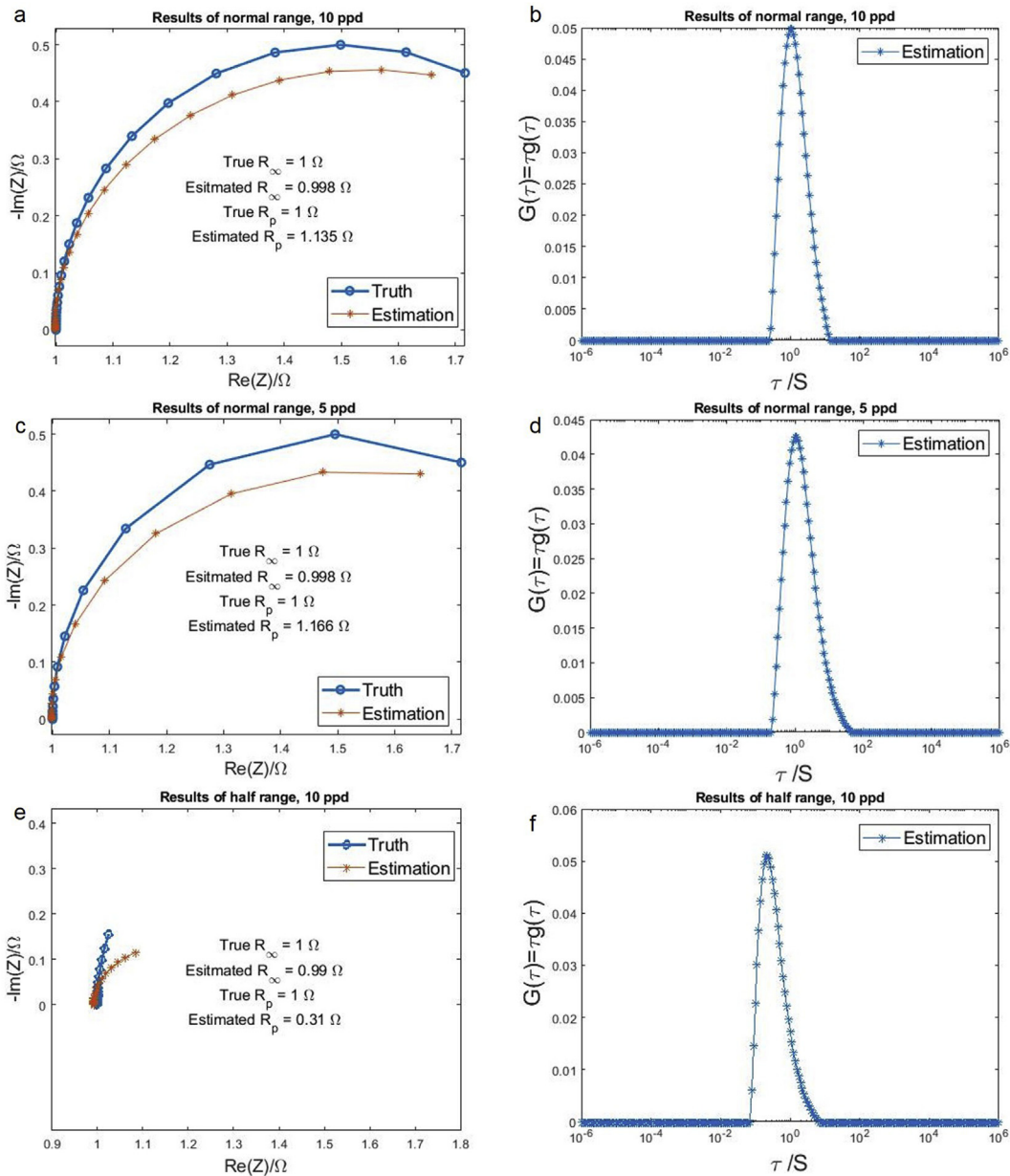


Fig. 6. Reconstructions of a RC circuit. (a,c,e) Analytical and estimated EIS spectra and resistances for the three data collection strategies: normal range with 10 ppd, normal range with 5 ppd, half range with 10 ppd. (b,d,f) Estimated DRTs, corresponding to the three data collection strategies.

and DRT were not affected, with estimated $L_0 = 0 \mu\text{H}$. For example, Fig. 11 is the fitting results for the full synthetic EIS data of ZARC mixtures with equal peaks in section 3.1.2. Ongoing work involving a more comprehensive investigation of the extended formalism including more experimental EIS datasets containing inductive effects is underway.

3.2.2. Synergistic DRT-ECM analysis

Although τ is continuously distributed, one has to discretize the domain of $G(\tau)$ in practice. We approximate $G(\tau)$ into the weighted mixtures of kernel functions. A kernel function has local effects on a certain interval $[\tau_m, \tau_{m+1}]$. It gives approximated/average EIS information on the interval $[\tau_m, \tau_{m+1}]$ and naturally contains variance, which could be the reason of the larger discrepancy between original data and reconstructed impedance at the low-frequency end as shown in Fig. 10a.

With that being said, estimated DRT could provide prior information on the number, type and initial parameters of ECM elements where those parameters can be further refined to improve the fitting of impedance data. To validate our hypothesis, based on the shape of estimated DRT, we fit the battery impedance data via a RQ(left peak)-RC(middle peak)-RC(right peak) mixture.

$$Z(f) = R_\infty + i2\pi fL + \frac{G_1}{1 + (i2\pi f\tau'_1)^{\phi_1}} + \frac{G_2}{1 + i2\pi f\tau'_2} + \frac{G_3}{1 + i2\pi f\tau'_3} \quad (29)$$

we use off-the-shelf lsqcurvefit function in MATLAB optimization tool-box to fit the nonlinear complex function. For a successful reconstruction, it is essential and non-trivial to find good initial points. And DRT is valuable for providing such key information. Fig. 12a shows the fitted impedance data from the ECM analysis with initial guesses based on the peak positions of DRT in Fig. 10b

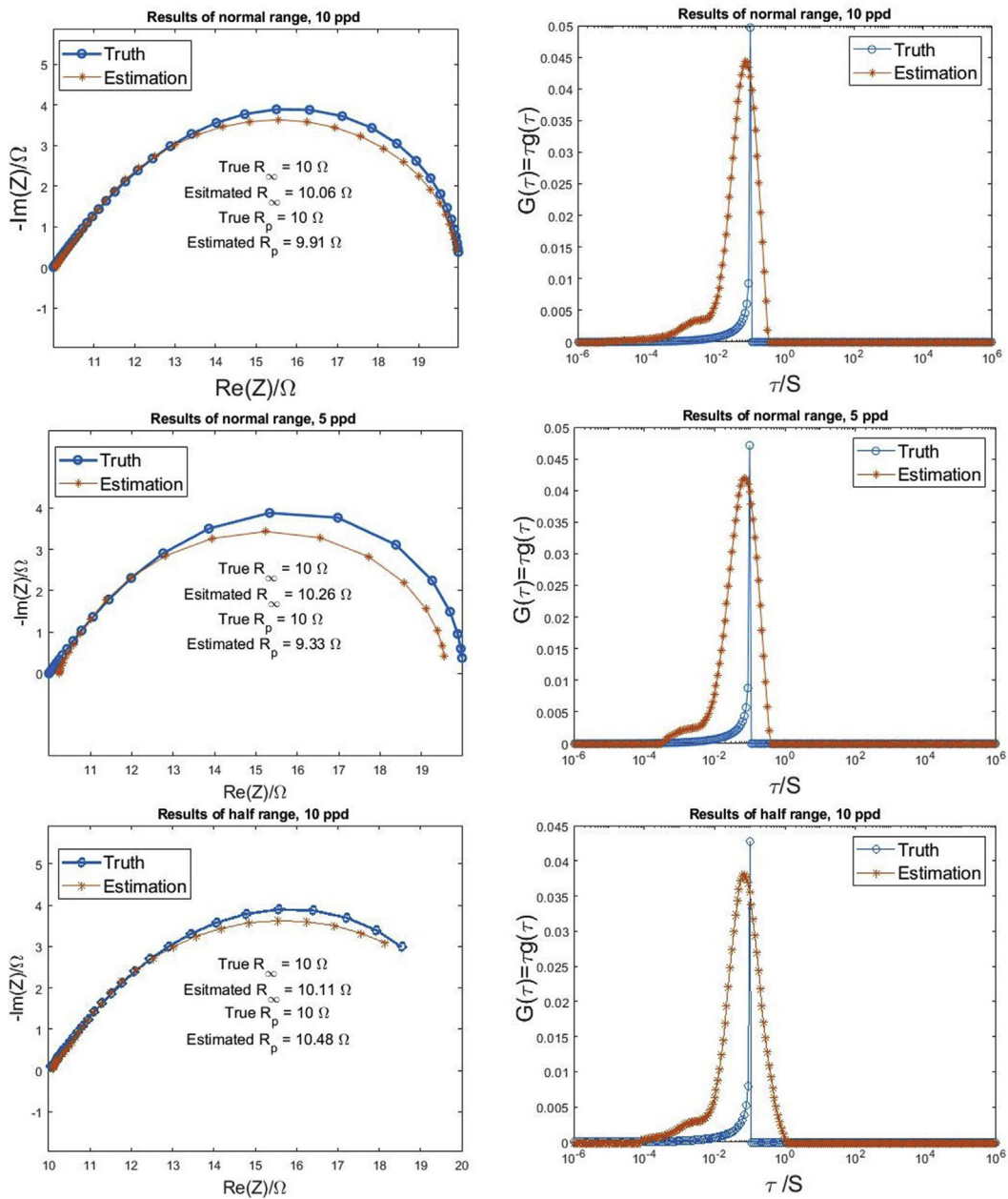


Fig. 7. Reconstructions of a Fractal element. (a,c,e) Analytical and estimated EIS spectra and resistances for the three data collection strategies: normal range with 10 pfd, normal range with 5 pfd, half range with 10 pfd. (b,d,f) Analytical and estimated DRTs, corresponding to the three data collection strategies.

($\tau_1 = 0.0015\text{s}$, $\tau_2 = 0.1571\text{s}$ and $\tau_3 = 32.77\text{s}$). The reconstruction of impedance was much improved via the refined ECM model based on DRT with parameter estimates: $G_1 = 0.0259\Omega$, $G_2 = 0.0106\Omega$, $G_3 = 0.0252\Omega$, $\tau'_1 = 0.0209\text{s}$, $\phi_1 = 0.2963$, $\tau'_2 = 0.1497\text{s}$, $\tau'_3 = 35.5382\text{s}$. We note that the discretized domain of DRT does not contain the exact sampling points at the refined characteristic relaxation times τ'_1 , τ'_2 , τ'_3 . Fig. 12b is a failure example of ECM fitting from random initial guesses of characteristic relaxation times. From the DRT-ECM analysis perspective, it is important to put structural-sparsity regularizations on the DRT to avoid overfitting. For example, Fig. 13 shows the overfitted results of the simulated Fractal element via Tikhonov regularization. Although impedance data was much better fitted in Fig. 13a than those in section 3.1.4, the corresponding DRT in Fig. 13b containing sharp pseudo-peaks is more indicative of a serial connection of multiple

RC-elements (or RQ-RC combinations).

3.3. EIS data analysis of organic-inorganic halide class of perovskites

Organic-inorganic halide class of perovskites (OIHPs) have recently come to the forefront of research curiosity due to their outstanding optoelectronic properties which make them suitable for a broad applications ranging from solar cells [64] to ionizing radiation detectors [65]. It is well established that these materials are mixed ionic-electronic conductors which makes the understanding of their charge transport properties under different operation condition challenging [66]. Hence, EIS has been widely used to characterize and decouple frequency dependent ionic and electronic processes in this class of materials [67,68]. Several groups

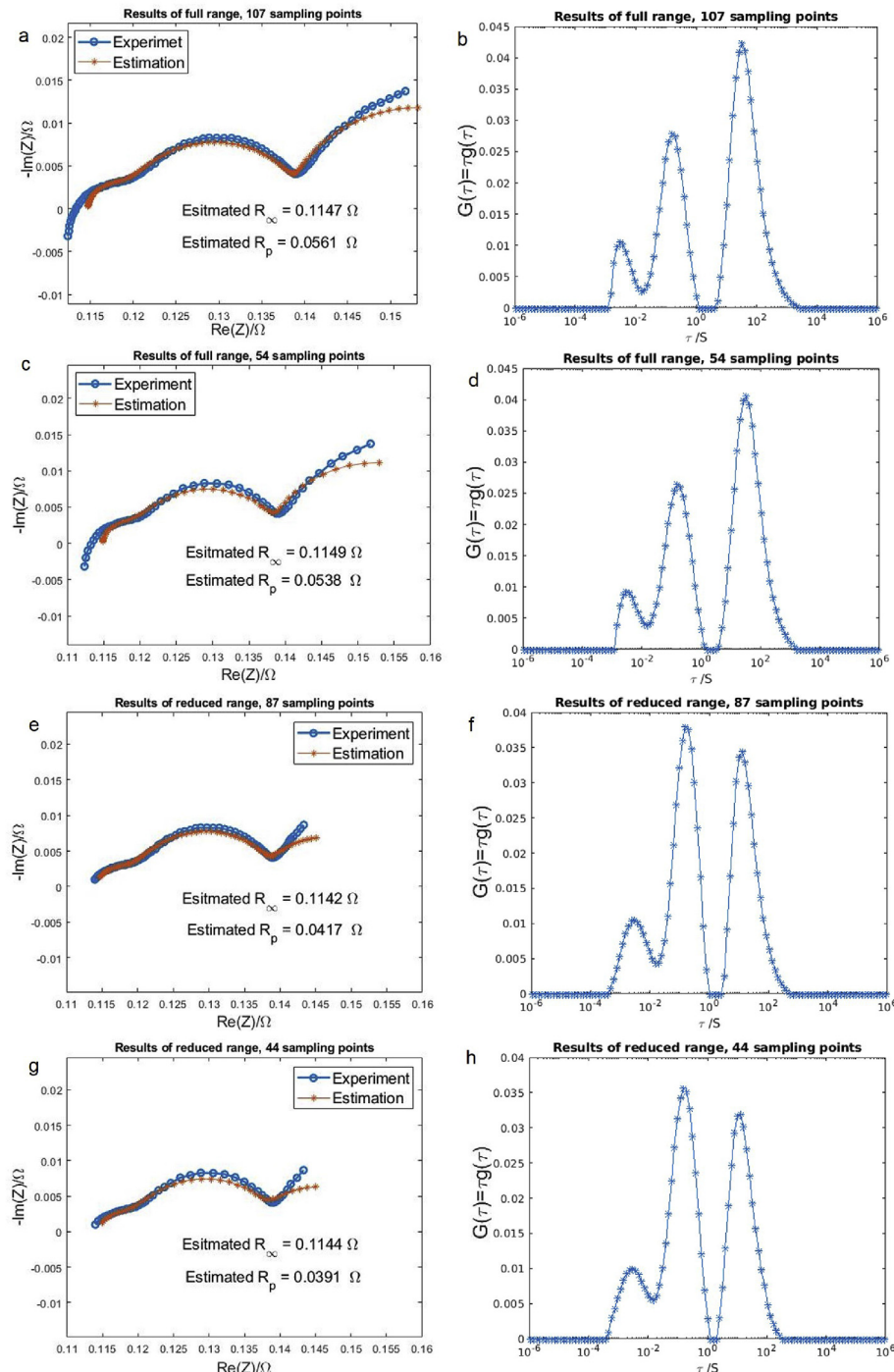


Fig. 8. Reconstructions of a Lithium ion battery EIS data. (a,c,e,g) Experimental and estimated EIS spectra and resistances for the four data collection strategies: full range, full range with half sampling density, reduced range and reduced range with half sampling density. (b,d,f,h) Estimated DRTs, corresponding to the four data collection strategies.

have used the equivalent circuit model to explain the origin of phenomena based on capacitive, resistive or inductive circuit elements. However, complex systems including OIHPs deviate from ideal resistor or capacitor structures and may not be described well with these elements. This complicates the interpretation of phenomena.

Here, we employed our DRT method for the first time to look at distribution of relaxation times on a single crystal of methylammonium lead bromide (MAPbBr₃) sandwich between Au electrodes in O₂ environment at different gas pressures. Similar to the

data setups in Lithium ion battery example, we considered four sampling strategies: (1) Full frequency range (450 kHz–2 Hz) with 197 sampling points; (2) Full frequency range (450 kHz–2 Hz) with half sampling density, yielding 99 sampling points; (3) Reduced frequency range (95 kHz–11 Hz) with 147 sampling points; (4) Reduced frequency range (95 kHz to 11 Hz) with half sampling density, yielding 74 sampling points. Fig. 14 and Fig. 15 are the fitting results, where we can see the reconstruction performances are consistent under these four data sampling strategies.

While understanding the origins of the phenomena is out of the

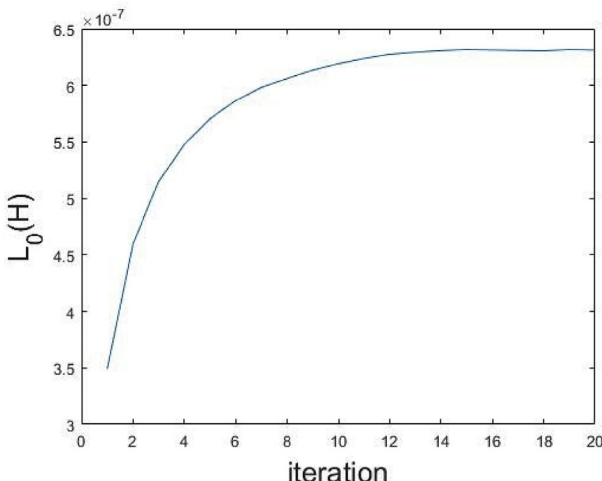


Fig. 9. An example of L_0 estimates during iterations for the Lithium-ion battery EIS data analysis.

scope of this paper, we can separately analyze each phenomenon based on their individual time scale. Clearly there are two individual processes with relaxation times in the orders of milliseconds (as indicated by peak P1 in Fig. 14b) and microseconds (as indicated by peak P2 in Fig. 14b). A recent study [69] on interaction of oxygen with halide perovskites has shown that, as the rate of absorption increases by increasing gas pressure, O_2 can change the concentration of charges and affect sample conductivity. Correspondingly,

the evolution of estimated DRTs can also reflect the effects of increasing O_2 pressure. First, the fast process (P2) shifted to a smaller value as pressure increases (inset in Fig. 14b): at low pressure 0 torr and 40 torr, P2 is centered at 5.744 μ s; at high pressure 120 torr and 200 torr, P2 is centered at 4.554 μ s. Second, the width of slower process (P1) shrinks as pressure increases. In terms of a ZARC element, shrinkage of peak width reflects the increase of the diffusion related constant ϕ in equation (18), based on which, one may conjecture that the element associated with P1 tends to transit from a constant phase element to a pure capacitance [36]. Third, the estimated overall polarization resistance decreases as O_2 pressure increases from 0 torr to 200 torr, reaching at 550.55 k Ω , 509.59 k Ω , 438.17 k Ω and 438.60 k Ω . The above transitions in DRT and resistances may be attributed to recombination of electronic charge carriers with increasing O_2 pressure.

3.4. Software release

To help readers better understand the approach and provide a convenient tool for EIS-DRT community, datasets and MATLAB codes for the statistical model selection algorithm and analysis will be freely available at the following address, <https://github.com/nonmin/EIS-DRT>. Equivalent implementations in opensource language Python may also be available soon.

4. Discussion

We formulate the estimation of distribution of relaxation time and resistances from EIS data as a statistical model selection problem based on the elastic net regularization simultaneously

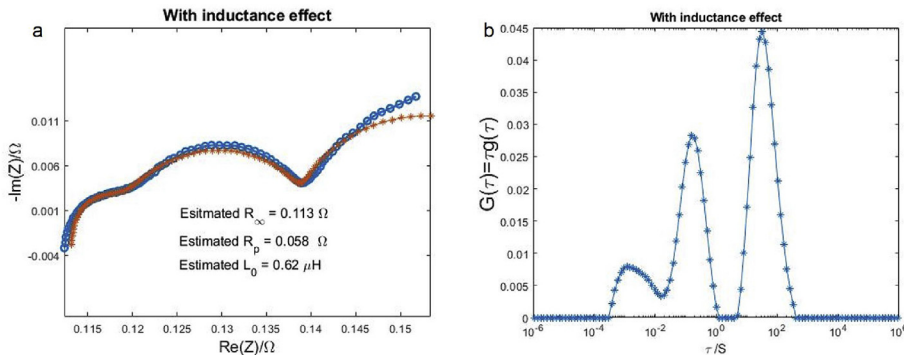


Fig. 10. Reconstructions of the full Lithium ion battery EIS data via the extended DRT model containing the inductance element. (a) Experimental and estimated EIS spectra. (b) Estimated DRT.

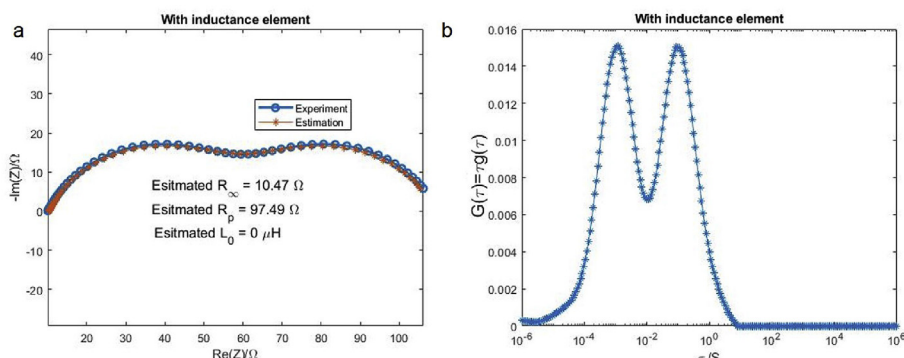


Fig. 11. Reconstructions of ZARC mixtures with equal weights, via the extended DRT model containing the inductance element. (a) Analytical and estimated EIS spectra. (b) Estimated DRT.

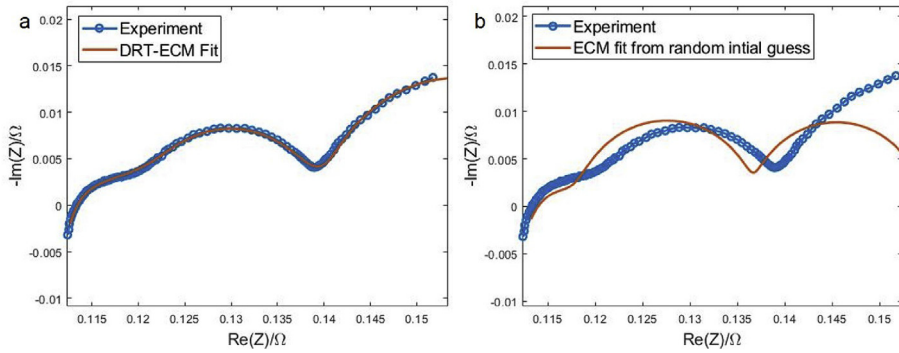


Fig. 12. ECM fitting of battery impedance based on DRT estimates and random initial guesses.

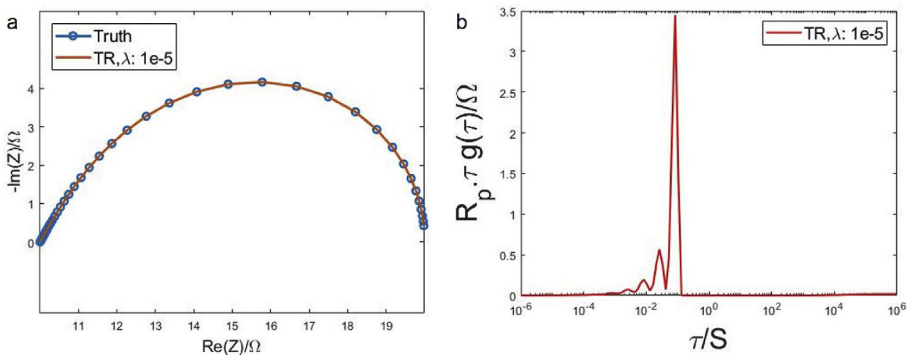


Fig. 13. An overfitting example of Fractal element via Tikhonov regularization.

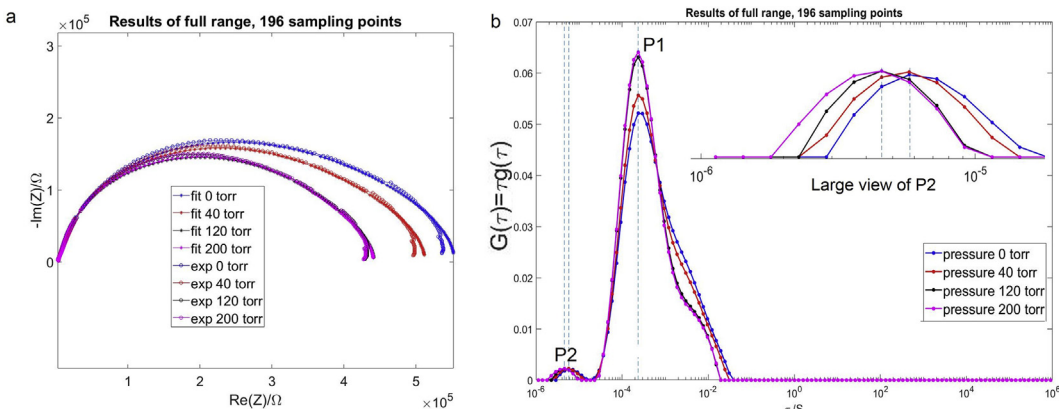


Fig. 14. Reconstructions of the EIS data from a single crystal of methylammonium lead bromide (MAPbBr₃) sandwich between Au electrodes in O₂ environment at different gas pressures. (a) Experimental and estimated EIS spectra for the data collection strategy: full range with 196 sampling points. (b) Estimated DRTs. Inset is the large view of the fast process.

taking advantages of Ridge and Lasso penalties. Based on the non-negative least angle regression algorithm (LARS), we propose a solving procedure that synergistically utilizes real- and imaginary-part of EIS data and automatically selects optimal tuning parameters based on information criterion.

We applied the model selection algorithm to four synthetic experiments of classical characteristics (a ZARC element, ZARC mixtures, a RC circuit and a Fractal element) and two real EIS datasets. We demonstrate our approach is capable of not only accurately estimating resistances but also suppressing pseudo peaks and representing asymmetry in the DRT. For the Lithium ion

battery data analysis, we extend the classical DRT model to incorporate the inductive effect and illustrate DRT as a guidance tool for equivalent circuit modeling to refine impedance reconstruction at low risks of overfitting. We highlight our approach is robust to reducing and subsampling EIS frequency range, showing potential for data analysis in emerging EIS techniques, such as timing-resolved [43–45], localized [46–48] and the atomic force microscopy based impedance spectroscopy [49–51], where EIS frequency range and sampling density may be limited by the spatial-temporal resolution and probe size.

Although this work only considers regression of a single EIS data

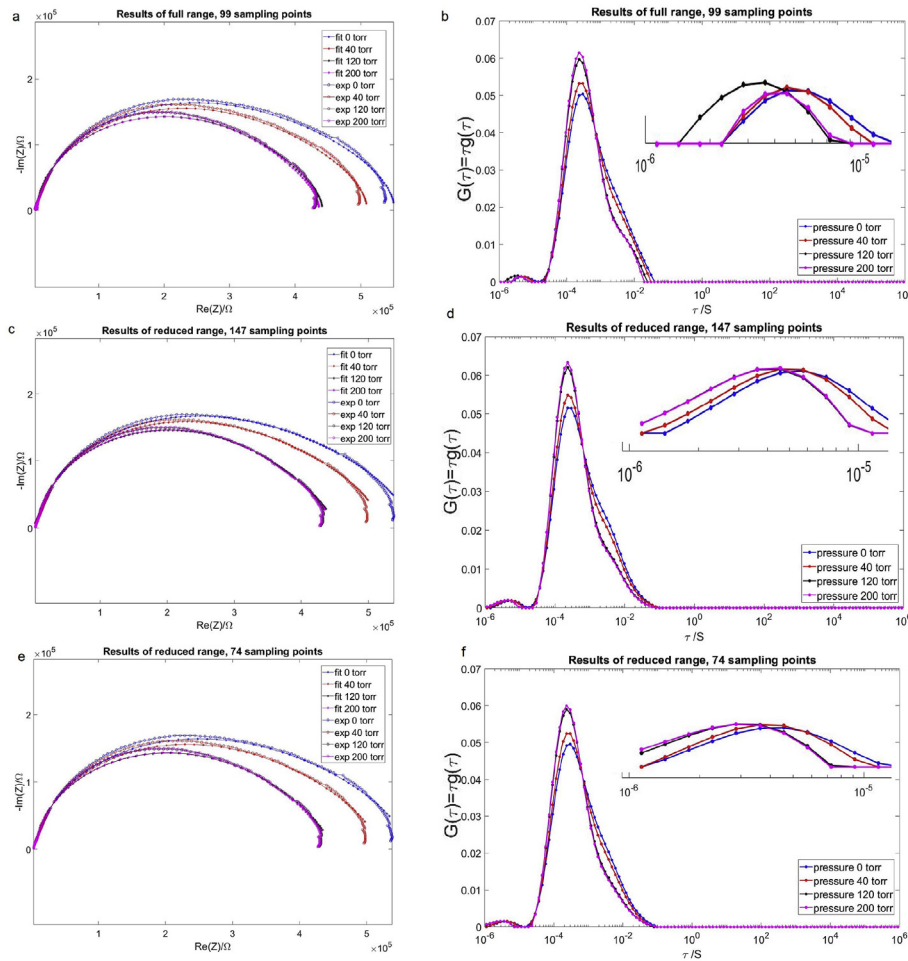


Fig. 15. Reconstructions of the EIS data from a single crystal of methylammonium lead bromide (MAPbBr₃) sandwich between Au electrodes in O₂ environment at different gas pressures. (a,c,e) Experimental and estimated EIS spectra for the three data collection strategies: full range with half sampling density, reduced range and reduced range with half sampling density. (b,d,f) Estimated DRTs, corresponding to the three data collection strategies. Inset is the large view of the fast process.

based on the one-dimensional elastic net sparsity penalization, the statistical model selection framework could naturally incorporate more elaborated structural-sparsity regularizations [70–72] for multi-dimensional and large-scale EIS data analysis [52,73]. The benefits of structural-sparsity such as elastic net could be explored further under the scope of Bayesian DRT analysis [53,54] via prior models such as spike and slab prior [55].

Acknowledgments

The research was performed at the Center for Nanophase Materials Sciences, a U.S. Department of Energy, Office of Science User Facility at Oak Ridge National Laboratory. M.A. acknowledges faculty start-up grant from the University of Tennessee, Knoxville.

References

- [1] A. Lasia, *Electrochemical impedance spectroscopy and its applications*, in: *Modern Aspects of Electrochemistry*, Springer, 2002, pp. 143–248, 2002.
- [2] E. Barsoukov, J.R. Macdonald, *Impedance Spectroscopy: Theory, Experiment, and Applications*, John Wiley & Sons, 2018, 2018.
- [3] Z. He, F. Mansfeld, Exploring the use of electrochemical impedance spectroscopy (eis) in microbial fuel cell studies, *Energy Environ. Sci.* 2 (2) (2009) 215–219, 2009.
- [4] G.M. Rupp, A.K. Opitz, A. Nenning, A. Limbeck, J. Fleig, Real-time impedance monitoring of oxygen reduction during surface modification of thin film cathodes, *Nat. Mater.* 16 (6) (2017) 640, 2017.
- [5] J.P. Schmidt, T. Chrobak, M. Ender, J. Illig, D. Klotz, E. Ivers-Tiffée, Studies on LiFePO₄ as cathode material using impedance spectroscopy, *J. Power Sources* 196 (12) (2011) 5342–5348, 2011.
- [6] J.P. Schmidt, P. Berg, M. Schönleber, A. Weber, E. Ivers-Tiffée, The distribution of relaxation times as basis for generalized time-domain models for li-ion batteries, *J. Power Sources* 221 (2013) 70–77, 2013.
- [7] Q. Wang, J.-E. Moser, M. Grätzel, Electrochemical impedance spectroscopic analysis of dye-sensitized solar cells, *J. Phys. Chem. B* 109 (31) (2005) 14945–14953, 2005.
- [8] F. Fabregat-Santiago, J. Bisquert, G. García-Belmonte, G. Boschloo, A. Hagfeldt, Influence of electrolyte in transport and recombination in dye-sensitized solar cells studied by impedance spectroscopy, *Sol. Energy Mater. Sol. Cell.* 87 (1–4) (2005) 117–131, 2005.
- [9] E.P. Randviir, C.E. Banks, Electrochemical impedance spectroscopy: an overview of bioanalytical applications, *Analytical Methods* 5 (5) (2013) 1098–1115, 2013.
- [10] K. Wapenaar, J. Schoonman, Conductivity enhancement in Ba_{1-x}LaxF_{2+x} solid electrolytes, *Solid State Ionics* 5 (1981) 637–640, 1981.
- [11] B.A. Boukamp, A nonlinear least squares fit procedure for analysis of imittance data of electrochemical systems, *Solid State Ionics* 20 (1) (1986) 31–44, 1986.
- [12] J.R. Macdonald, L.D. Potter Jr., A flexible procedure for analyzing impedance spectroscopy results: description and illustrations, *Solid State Ionics* 24 (1) (1987) 61–79, 1987.
- [13] J. Dugas, G. Fafilek, H. Durakpasa, M. Breiter, Automated setup for impedance measurements of electrochemical cells with two electrodes, *J. Appl. Electrochem.* 23 (6) (1993) 553–558, 1993.
- [14] B.A. Boukamp, Electrochemical impedance spectroscopy in solid state ionics: recent advances, *Solid State Ionics* 169 (1–4) (2004) 65–73, 2004.
- [15] J.R. Macdonald, D.R. Franceschetti, Precision of impedance spectroscopy estimates of bulk, reaction rate, and diffusion parameters, *J. Electroanal. Chem. Interfacial Electrochem.* 307 (1–2) (1991) 1–11, 1991.
- [16] S.B. Adler, J. Lane, B. Steele, Electrode kinetics of porous mixed-conducting oxygen electrodes, *J. Electrochem. Soc.* 143 (11) (1996) 3554–3564, 1996.

- [17] S.B. Adler, Mechanism and kinetics of oxygen reduction on porous $\text{La}_{1-\delta}\text{Sr}_{x}\text{CoO}_3-\delta$ electrodes, *Solid State Ionics* 111 (1–2) (1998) 125–134, 1998.
- [18] J. Jamnik, J. Maier, Generalised equivalent circuits for mass and charge transport: chemical capacitance and its implications, *Phys. Chem. Chem. Phys.* 3 (9) (2001) 1668–1678, 2001.
- [19] S. Adler, Reference electrode placement in thin solid electrolytes, *J. Electrochim. Soc.* 149 (5) (2002) E166–E172, 2002.
- [20] W. Lai, S.M. Haile, Impedance spectroscopy as a tool for chemical and electrochemical analysis of mixed conductors: a case study of ceria, *J. Am. Ceram. Soc.* 88 (11) (2005) 2979–2997, 2005.
- [21] Y. Lu, C. Kreller, S.B. Adler, Measurement and modeling of the impedance characteristics of porous $\text{La}_{1-x}\text{Sr}_x\text{CoO}_3-\delta$ electrodes, *J. Electrochim. Soc.* 156 (4) (2009) B513–B525, 2009.
- [22] F. Ciucci, W.C. Chueh, D.G. Goodwin, S.M. Haile, Surface reaction and transport in mixed conductors with electrochemically-active surfaces: a 2-d numerical study of ceria, *Phys. Chem. Chem. Phys.* 13 (6) (2011) 2121–2135, 2011.
- [23] C. Chen, D. Chen, W.C. Chueh, F. Ciucci, Modeling the impedance response of mixed-conducting thin film electrodes, *Phys. Chem. Chem. Phys.* 16 (23) (2014) 11573–11583, 2014.
- [24] E. Ivers-Tiffée, A. Weber, Evaluation of electrochemical impedance spectra by the distribution of relaxation times, *J. Ceram. Soc. Jpn.* 125 (4) (2017) 193–201, 2017.
- [25] K. Kobayashi, T.S. Suzuki, Distribution of relaxation time analysis for non-ideal admittance spectrum: discussion and progress, *J. Phys. Soc. Jpn.* 87 (9) (2018), 094002, 2018.
- [26] B.A. Boukamp, A. Rolle, Analysis and application of distribution of relaxation times in solid state ionics, *Solid State Ionics* 302 (2017) 12–18, 2017.
- [27] A. Franklin, H. De Bruin, The fourier analysis of impedance spectra for electrode-doped solid electrolytes, *Phys. Status Solidi* 75 (2) (1983) 647–656, 1983.
- [28] H. Schichlein, A.C. Müller, M. Voigts, A. Krügel, E. Ivers-Tiffée, Deconvolution of electrochemical impedance spectra for the identification of electrode reaction mechanisms in solid oxide fuel cells, *J. Appl. Electrochim.* 32 (8) (2002) 875–882, 2002.
- [29] R.M. Fuoss, J.G. Kirkwood, Electrical properties of solids. viii. dipole moments in polyvinyl chloride-diphenyl systems, *J. Am. Chem. Soc.* 63 (2) (1941) 385–394, 1941.
- [30] B.A. Boukamp, Fourier transform distribution function of relaxation times: application and limitations, *Electrochim. Acta* 154 (2015) 35–46, 2015.
- [31] T. Hörlin, Deconvolution and maximum entropy in impedance spectroscopy of noninductive systems, *Solid State Ionics* 107 (3–4) (1998) 241–253, 1998.
- [32] J.R. Macdonald, Comparison of parametric and nonparametric methods for the analysis and inversion of admittance data: critique of earlier work, *J. Comput. Phys.* 157 (1) (2000) 280–301, 2000.
- [33] E. Tuncer, S. Gubanski, On dielectric data analysis. using the Monte Carlo method to obtain relaxation time distribution and comparing non-linear spectral function fits, *IEEE Trans. Dielectr. Electr. Insul.* 8 (3) (2001) 310–320, 2001.
- [34] S. Hershkovitz, S. Baltianski, Y. Tsur, Harnessing evolutionary programming for impedance spectroscopy analysis: a case study of mixed ionic-electronic conductors, *Solid State Ionics* 188 (1) (2011) 104–109, 2011.
- [35] A. Tesler, D. Lewin, S. Baltianski, Y. Tsur, Analyzing results of impedance spectroscopy using novel evolutionary programming techniques, *J. Electroceram.* 24 (4) (2010) 245–260, 2010.
- [36] F. Dion, A. Lasia, The use of regularization methods in the deconvolution of underlying distributions in electrochemical processes, *J. Electroanal. Chem.* 475 (1) (1999) 28–37, 1999.
- [37] M. Saccoccio, T.H. Wan, C. Chen, F. Ciucci, Optimal regularization in distribution of relaxation times applied to electrochemical impedance spectroscopy: Ridge and lasso regression methods-a theoretical and experimental study, *Electrochim. Acta* 147 (2014) 470–482, 2014.
- [38] T.H. Wan, M. Saccoccio, C. Chen, F. Ciucci, Influence of the discretization methods on the distribution of relaxation times deconvolution: implementing radial basis functions with DRT tools, *Electrochim. Acta* 184 (2015) 483–499, 2015.
- [39] Y. Zhang, Y. Chen, M. Li, M. Yan, M. Ni, C. Xia, A high-precision approach to reconstruct distribution of relaxation times from electrochemical impedance spectroscopy, *J. Power Sources* 308 (2016) 1–6, 2016.
- [40] A. Gavriluk, D. Osinkin, D. Bronin, The use of tikhonov regularization method for calculating the distribution function of relaxation times in impedance spectroscopy, *Russ. J. Electrochim.* 53 (6) (2017) 575–588, 2017.
- [41] J.R. Macdonald, Impedance spectroscopy: old problems and new developments, *Electrochim. Acta* 35 (10) (1990) 1483–1492, 1990.
- [42] F. Ciucci, Modeling electrochemical impedance spectroscopy, *Current Opinion in Electrochemistry* 13 (February 2019) 132–139.
- [43] H. Zappen, F. Ringbeck, D. Sauer, Application of time-resolved multi-sine impedance spectroscopy for lithium-ion battery characterization, *Batteries* 4 (4) (2018) 64, 2018.
- [44] J. Glenneberg, I. Bardenhagen, F. Langer, M. Busse, R. Kun, Time resolved impedance spectroscopy analysis of lithium phosphorous oxynitride-lipon layers under mechanical stress, *J. Power Sources* 359 (2017) 157–165, 2017.
- [45] R. Srinivasan, B.G. Carkhuff, M.H. Butler, A.C. Baisden, Instantaneous measurement of the internal temperature in lithium-ion rechargeable cells, *Electrochim. Acta* 56 (17) (2011) 6198–6204, 2011.
- [46] D. Trinh, M. Keddam, X.R. Novoa, V. Vivier, Characterization of adsorbates by transient measurements in scanning electrochemical microscopy, *Electrochim. Acta* 131 (2014) 28–35, 2014.
- [47] V. Shkirskiy, P. Volovitch, V. Vivier, Development of quantitative local electrochemical impedance mapping: an efficient tool for the evaluation of delamination kinetics, *Electrochim. Acta* 235 (2017) 442–452, 2017.
- [48] C.P. de Abreu, C.M. de Assis, P.H. Suegama, I. Costa, M. Keddam, H.G. de Melo, V. Vivier, Influence of probe size for local electrochemical impedance measurements, *Electrochim. Acta* 233 (2017) 256–261, 2017.
- [49] R. OHayre, M. Lee, F.B. Prinz, Ionic and electronic impedance imaging using atomic force microscopy, *J. Appl. Phys.* 95 (12) (2004) 8382–8392, 2004.
- [50] E. Strelcov, S. Jesse, Y.-L. Huang, Y.-C. Teng, I.I. Kravchenko, Y.-H. Chu, S.V. Kalinin, Space-and time-resolved mapping of ionic dynamic and electroresistive phenomena in lateral devices, *ACS Nano* 7 (8) (2013) 6806–6815, 2013.
- [51] J. Izquierdo, B. Fernández-Pérez, A. Eifert, R. Souto, C. Kranz, Simultaneous atomic force scanning electrochemical microscopy (afm-secm) imaging of copper dissolution, *Electrochim. Acta* 201 (2016) 320–332, 2016.
- [52] A. Mertens, J. Granwehr, Two-dimensional impedance data analysis by the distribution of relaxation times, *Journal of Energy Storage* 13 (2017) 401–408, 2017.
- [53] F. Ciucci, C. Chen, Analysis of electrochemical impedance spectroscopy data using the distribution of relaxation times: a bayesian and hierarchical bayesian approach, *Electrochim. Acta* 167 (2015) 439–454, 2015.
- [54] M.B. Efrat, F. Ciucci, Bayesian and hierarchical bayesian based regularization for deconvolving the distribution of relaxation times from electrochemical impedance spectroscopy data, *Electrochim. Acta* 247 (2017) 1117–1129, 2017.
- [55] H. Ishwaran, J.S. Rao, et al., Spike and slab variable selection: frequentist and bayesian strategies, *Ann. Stat.* 33 (2) (2005) 730–773, 2005.
- [56] X. Li, P.H. Tran, T. Liu, C. Park, Simulation-guided regression approach for estimating the size distribution of nanoparticles with dynamic light scattering data, *IIE Transactions* 49 (1) (2017) 70–83, 2017.
- [57] H. Zou, T. Hastie, Regularization and variable selection via the elastic net, *J. R. Stat. Soc. Ser. B* 67 (2) (2005) 301–320, 2005.
- [58] B. Efron, T. Hastie, I. Johnstone, R. Tibshirani, et al., Least angle regression, *Ann. Stat.* 32 (2) (2004) 407–499, 2004.
- [59] M. Slawski, M. Hein, et al., Non-negative least squares for high-dimensional linear models: consistency and sparse recovery without regularization, *Electronic Journal of Statistics* 7 (2013) 3004–3056, 2013.
- [60] C.L. Mallows, Some comments on c p, *Technometrics* 15 (4) (1973) 661–675, 1973.
- [61] K.S. Cole, R.H. Cole, Dispersion and absorption in dielectrics i. alternating current characteristics, *J. Chem. Phys.* 9 (4) (1941) 341–351, 1941.
- [62] R. De Levie, On the impedance of electrodes with rough interfaces, *J. Electroanal. Chem. Interfacial Electrochem.* 261 (1) (1989) 1–9, 1989.
- [63] C.L. Lawson, R.J. Hanson, Solving Least Squares Problems, vol. 15, Siam, 1995, p. 1995.
- [64] D. Yang, R. Yang, K. Wang, C. Wu, X. Zhu, J. Feng, X. Ren, G. Fang, S. Priya, S.F. Liu, High efficiency planar-type perovskite solar cells with negligible hysteresis using edta-complexed sno 2, *Nat. Commun.* 9 (1) (2018) 3239, 2018.
- [65] J.T. Tisdale, T. Smith, J.R. Salasin, M. Ahmadi, N. Johnson, A.V. Ievlev, M. Koehler, C.J. Rawn, E. Lukosi, B. Hu, Precursor purity effects on solution-based growth of mapbr 3 single crystals towards efficient radiation sensing, *CrystEngComm* 20 (48) (2018) 7818–7825, 2018.
- [66] W. Tress, Metal halide perovskites as mixed electronic–ionic conductors: challenges and opportunities from hysteresis to memristivity, *J. Phys. Chem. Lett.* 8 (13) (2017) 3106–3114, 2017.
- [67] A.R. Pascoe, N.W. Duffy, A.D. Scully, F. Huang, Y.-B. Cheng, Insights into planar $\text{CH}_3\text{NH}_3\text{PbI}_3$ perovskite solar cells using impedance spectroscopy, *J. Phys. Chem. C* 119 (9) (2015) 4444–4453, 2015.
- [68] O. Vyunov, A. Belous, S. Kobylanska, L. Kovalenko, Impedance analysis of thin films of organic-inorganic perovskites $\text{CH}_3\text{NH}_3\text{PbI}_3$ with control of microstructure, *Nanoscale research letters* 13 (1) (2018) 98, 2018.
- [69] A. Senocrate, T. Acartürk, G.Y. Kim, R. Merkle, U. Starke, M. Grätzel, J. Maier, Interaction of oxygen with halide perovskites, *J. Mater. Chem. B* (23) (2018) 10847–10855, 2018.
- [70] Y. She, Sparse regression with exact clustering, *Electronic Journal of Statistics* 4 (2010) 1055–1096, 2010.
- [71] J. Huang, T. Zhang, D. Metaxas, Learning with structured sparsity, *J. Mach. Learn. Res.* 12 (Nov) (2011) 3371–3412, 2011.
- [72] X. Li, A. Belianinov, O. Dyck, S. Jesse, C. Park, et al., Two-level structural sparsity regularization for identifying lattices and defects in noisy images, *Ann. Appl. Stat.* 12 (1) (2018) 348–377, 2018.
- [73] A.S. Bondarenko, Analysis of large experimental datasets in electrochemical impedance spectroscopy, *Anal. Chim. Acta* 743 (2012) 41–50, 2012.